A Modified Positive Velocity and Position Feedback scheme with delay compensation for improved nanopositioning performance

Andres San-Millan[1], Douglas Russell[2], Vicente Feliu[3] and Sumeet S. Aphale[4]

[1,3] University of Castilla-La Mancha, Ciudad Real 13071, Spain. [2,4] Center for Applied Dynamics Research, School of Engineering, University of Aberdeen, Aberdeen, AB24 3UE, U.K.

E-mail: [1] andres.sanmillan@uclm.es, [2] r01dr12@abdn.ac.uk, [3] vicente.feliu@uclm.es, [4] s.aphale@abdn.ac.uk

Abstract.

This paper presents a controller design to compensate the effects of time delay in a flexure-based piezoelectric stack driven nanopositioner. The effects of the time delay in flexure nanopositioners is illustrated and identified by means of experimentally obtaining the frequency response of the system. Moreover, a theoretical model which takes into account the dependence between the sampling time and the delay introduced is proposed. The proposed control design methodology not only accommodates for time delay but also ensures the robust stability and allows its application to systems with a larger delay than other schemes proposed previously. Limitations and future work are discussed.

PACS numbers: 68.37.Ps,85.50.-n, 02.30.Ks, 43.40.Vn

Keywords: high-speed atomic force microscope (AFM), flexure guided nanopositioner, piezoelectric actuators, Positive Velocity and Position Feedback (PVPF), time delay, tracking , Active vibration control Submitted to: *Smart Materials and Structures*

1. Introduction

Nanopositioners generally come in two types viz: tube-type and platform-type, which predominantly employ piezoelectric actuators due to their easy control and arbitrarily fine resolution [1]. The achievable resolution, which can be in the range of the atomic scale [2], makes nanopositioners widely applicable in atomic force microscopes (AFM), micro-/nanomanipulation [3], fiber optic alignment [4] and electrical characterization of semiconductors [5].

Due to the recently increased demand for high-speed AFM in the areas of imaging of fast biological processes [6], and video-rate AFM [7, 8, 9], piezoelectric tube scanners have been replaced by flexure-based piezoelectric stack driven nanopositioners. Among their advantages are low cross-coupling between motion axes, robust mechanical construction, large motion range and high mechanical bandwidth. However, the two main drawbacks of flexure-based mechanisms are: 1) the nonlinearity of piezoelectric actuators employed to drive the nanopositioner, and 2) their lightly damped resonance peaks, which impose an upper bound on the achievable bandwidth, determined by the first resonance mode of the nanopositioner.

Because of these drawbacks the nanopositioners are usually operated by means of different closed-loop control schemes [2], and several feedback control techniques have been successfully implemented to suppress vibration and compensate for nonlinearity, such as Positive Position Feedback (PPF) [10], polynomial-based control (also known as Positive Velocity and Position Feedback - PVPF) [11], Resonant control [12], robust control [13], and Integral Resonance Control (IRC) [14].

Flexure nanopositioners are typically composed of five components: a flexure-hinge-based mechanism, one or many piezoelectric actuators (PEAs), depending on the number of degrees of freedom (DOF) of the nanopositioner, a piezoelectric drive circuit for each PEA, a displacement sensor for each DOF, and an electronic control circuit, which executes the control algorithm.

While the identification, modelling, and control of the mechanical structure and the PEAs has attracted significant attention in the literature, the dynamics of the rest of the system, i.e. the piezoelectric drive circuit, the displacement sensor, and the electronic control circuit, is usually neglected because it is assumed that its dynamics are much faster in comparison to the mechanical part of the system.

However, the joint action of these three components may lead to the introduction of a time delay which becomes significant over the large bandwidth of the nanopositioning system. The existence of this delay, and its effect on nanopositioners was first noticed in [15]. In this work, the delay introduced by finite clock speeds of the signal conditioning circuitry associated with displacement sensors was quantified, and the stability conditions of the IRC scheme were extended to accommodate the effects of the delay by means of the Padé approximation.

In this paper, the delay introduced not only by the displacement sensors, but also by the electronic control circuit is quantified, and it is found that there exists a linear relationship between the sampling time and the delay introduced. Once the delay of the system is identified, it is included in the dynamical model of the nanopositioner. Then the methodology of design of the PVPF control scheme is extended to include such delay. This yields some analytically exact expressions which allow us to easily study the stability of the closed-loop system and determine the maximum delay admissible before running into instability. This modification of the traditional PVPF will be denoted "modified PVPF".

The identification of the relationship between the sampling time and the delay introduced together with the compensation of the effect of the delay allows the utilisation of slower sampling rates to control the nanopositioner. This relaxation in the sampling rate allows the utilisation of a wider range of electronic systems to control the nanopositioner and, therefore, potentially reduce the cost associated with the electronic control circuit.

It is important to note that traditional techniques for delay compensation such as Smith predictor [16], and direct inversion of plant dynamics are not applicable to flexure-based nanopositioners. The infinite number of unmodeled vibration modes prevents the application of the Smith predictor, and the direct inversion of plant dynamics is not possible as the time delay introduces non-minimum phase (NMP) zeros in the system which would lead to unstable poles. This is the reason why research into the quantification and compensation of the delay of the system is of utmost interest.

This article is organized as follows. In Section 2, the background theory regarding the modeling of

a nanopositioner including the delay is presented. In Section 3, the theoretical model of the PVPF controller and the methodology of parameter tuning for systems without time delay are presented. The inclusion of time delay in the model of the system, by means of a Padé approximation, and the subsequent compensation of its effects, utilising the modified PVPF control scheme, is presented in Section 4. In Section 5, the experimental platform is presented and the procedure employed for the experimental system identification is described. The experimental results, obtained for both the traditional and modified PVPF control schemes, are presented in Section 6. From these results it can be seen that the modified PVPF scheme achieves better performance than the traditional PVPF scheme when the nanopositioner presents a time delay. In Section 7, the robustness of both controllers is analysed by relating the value of the delay of the platform and the stability of the closed loop system. The maximum range of application of the modified PVPF control scheme is also analysed, showing that the maximum admissible delay in the plant is greater than with traditional PVPF. Finally, Section 8 presents some conclusions.

2. Background theory

In this section, the theoretical model utilised to capture the behaviour of the nanopositioner is presented. First, the equations utilised to reproduce the dynamics of the flexure-hinge-based mechanism are presented, and then the different elements which contribute to the introduction of a delay are listed. Finally, the dependence between the delay and the sampling time is justified.

2.1. Theoretical model of the mechanical structure

A two-axis flexure-based nanopositioner can be interpreted as a linear system with two inputs and two outputs $Y(s) = G(s)U(s)$, where $U(s)$ denotes the Laplace transform of $[V_x, V_y]^T$, the voltage signals applied to the piezoelectric drive circuits along the x and y directions, $Y(s)$ denotes the Laplace transform of $[D_x, D_y]^T$, the voltage signals read with the displacement sensors along the x and y directions, and

$$G(s) = \begin{bmatrix} G_{xx}(s) & G_{xy}(s) \\ G_{yx}(s) & G_{yy}(s) \end{bmatrix} \tag{1}$$

the transfer matrix relating the inputs and the outputs.

As mentioned in the introduction, the cross-coupling between the motion axes is very low and can be considered negligible, which means $G_{xy}(s) = G_{yx}(s) = 0$ (this hypothesis is confirmed in the section devoted to the analysis of the experimental platform). Furthermore, since only the $x-$axis of the platform was used to conduct experiments in this work, $G_{yy}(s) = 0$. Note that the $y-$axis was suitably biased and fed 0 V as input to mimic realistic platform operation.

Therefore, the studied system can be interpreted as $Y(s) = G(s)U(s)$, where $Y(s) = D_x(s)$, $G(s) = G_{xx}(s)$, and $U(s) = V_x(s)$. The input-output frequency response of the system can be represented by means of an infinite sum of second-order transfer-functions as follows:

$$G(s) = \sum_{i=1}^{M} \frac{\sigma_i^2}{s^2 + 2\zeta_i\omega_i s + \omega_i^2} \tag{2}$$

where $M \to \infty$, σ_i^2 corresponds to the gain of each mode of vibration, ζ_i is the damping ratio of each mode, and ω_i is the natural frequency of vibration of each mode. However, for practical purposes (2) is usually truncated to contain a finite number of modes. In several works [13, 15, 17, 18, 19], (2) is truncated at the first mode as it is dominant.

Since the design of the PVPF control scheme is based on a simplified model of the plant composed only by the first mode of vibration [19], in this article it is chosen $M = 1$. However, it is important to note that the error introduced in the model due to the truncation of the high-frequency modes, deems the Smith Predictor and direct plant dynamics inversion approach infeasible when compensating for the delay. Since both techniques rely on the knowledge of a full model of the plant, the higher order modes of vibration cannot be controlled and become unstable.

Note that according to [20], it has been mathematically verified that the dynamics of a PEA can be approximated as a second-order system, and the dynamics of the PEAs of the nanopositioner can therefore be included in (2). However, in [21] it was demonstrated that the typical resonance frequency of stack PEAs is usually over 50 times greater than the first mode of vibration of the mechanical structure of the nanopositioner, and lies therefore outside the bandwidth of interest.

2.2. Theoretical model of the electrical subsystem

The electrical subsystem of the nanopositioner is comprised of the piezoelectric drive circuit, the displacement sensor, and the electronic control circuit. These three components work sequentially in the following way: first, the displacement sensor reads the position of the nanopositioner, second, the signal is conditioned in the sensor and translated to a level of voltage suitable for use in the electronic control circuit, third, the analog signal available at the displacement sensor is digitized by the electronic control circuit, which utilizes that value as input for the control system (when the system is operated in closed loop), or just in

order to record the measured data (when the system is operated in open loop). Finally, the output of the electronic control circuit is converted to an analog signal which is applied to the piezoelectric drive circuit. This circuit raises the voltage level to the working voltage of the PEAs.

The aforementioned set of operations is repeated sequentially whether the system is operated in closed loop or in open loop. The time taken to repeat each cycle of the sequence is denoted cycle time, and since in each cycle the system is sampled once, it can be seen that the cycle time and the sampling time are equal, and both terms are used synonymously hereinafter. Note that the term "sampling rate"is the inverse of the sampling time.

This set of operations is not instantaneous due to physical limitations. The cumulative time taken to complete them produces a fixed amount of delay between the time instant at which the measurement is taken and the instant at which the action is applied. This is known as latency and its value is always lower than or equal to the cycle time, determining, therefore, a lower bound to the achievable sampling time. Note that the main sources of latency are the signal conditioning, the analog to digital conversion, the hardware communication (which includes all the processes necessary to transport the signal from the DAC into the software execution system), and the digital to analog conversion. The first source of latency was the reason pointed out in [15] for the apparition of a delay in the system, however we will show in this paper that there are several reasons, and that they are cumulative.

The latency of the system justifies the apparition of a fixed amount of delay in the system. However, according to [22, 23] the zero-order hold (which is extensively used in the digital to analog conversion stage) can be interpreted as a time delay element which introduces a delay equal to half the sampling period. Note that this property can be seen in the frequency-dependent phase response of the hold, which is the same technique utilised in [15] to identify the delay of the system. This property predicts a linear dependence between the sampling time and the delay introduced in the system. When both delays are considered, it can be seen that the total delay introduced in the system is composed by the sum of a fixed amount produced by the latency of the system and by a variable amount determined by the sampling period.

The traditional way to increase the sampling rate, and reduce the latency of the system (and therefore reduce the delay introduced) is the utilization of a custom, dedicated hardware implementation of the control algorithm such as a FPGA, a custom-built analog circuit, or PXI systems. However, these systems are less flexible and more expensive that the utilisation of software-dependent controllers. The software-dependent controllers are usually presented in the form of a traditional PC equipped with some real-time operating system and signal acquisition hardware [18, 24, 25]. This architecture is highly flexible due to its integration with very popular design and control software, such as Simulink or LabView, but the sampling periods achievable with such equipment are in the range of tens of microseconds, which makes the effect of the introduced delay not negligible.

It is important to note that a reduction in the sampling rate as a design constraint allows a reduction in the cost of the electronics components utilised to control the system, and an increase in the number of control electronics available for this application.

3. Traditional PVPF control scheme without delay compensation

In order to reduce the positioning errors in a nanopositioner and to impart substantial damping to the lightly-damped resonance mode, the polynomial-based pole-placement technique [26] has been widely employed in the form of three different control schemes: resonant controller, PPF, and PVPF. The PVPF design is composed of a closed-loop damping controller in conjunction with a suitably gained integral tracking controller. It is important to note that the integral tracking controller of the PVPF is utilised in order to reduce the tracking error produced by uncertainties in the mathematical model of the nanopositioner and by the nonlinearity of the actuators, and it must not be confused with the lossy integrator utilised in [14], which is utilised in order to to improve the stability margins of the IRC damping scheme.

Typically, both the damping and the tracking controllers are designed independently and sequentially [27]; damping controller first and then the tracking controller. However a design strategy was recently proposed in [19] in which the selection of the parameters for the PVPF controller as well as the integral gain were carried out simultaneously to achieve an optimal damping and tracking effect. The simple structure of the PVPF scheme, its ability to arbitrarily place the poles of the closed-loop system, and the possibility of achieving an optimal damping and tracking effect are the reasons why this control scheme is utilised in this work.

The structure of the PVPF controller is shown in Figure 1, where $R(s)$, is the Laplace transform of $r(t)$ (the reference applied to the closed-loop system), and $C_{damp}(s)$ and $C_{track}(s)$ are given by:

$$C_{damp}(s) = \frac{\Gamma_2 s + \Gamma_1}{s^2 + 2\gamma\omega_c s + \omega_c^2} \tag{3}$$

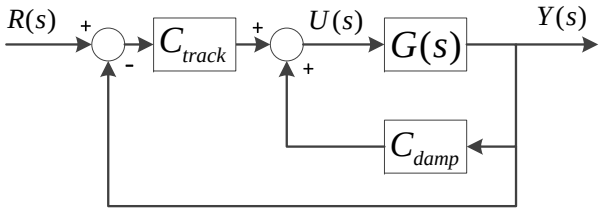

Figure 1. Block diagram of the closed-loop PVPF control scheme with tracking

$$C_{track}(s) = \frac{k_t}{s} \tag{4}$$

Considering only the first mode of vibration of the plant, and neglecting the time delay introduced, the nanopositioner can be modeled by the following equation:

$$G(s) = \frac{\sigma^2}{s^2 + 2\zeta\omega_n s + \omega_n^2} \tag{5}$$

The closed-loop transfer function, therefore, has the following expression: $Y(s)/R(s) = M_{num}(s)/M_{den}(s)$, where:

$$\begin{aligned} M_{num}(s) =& k_t\sigma^2(s^2 + 2\gamma\omega_c s + \omega_c^2) \\ M_{den}(s) =& s^5 + (2\zeta\omega_n + 2\gamma\omega_c)s^4 \\ &+ (2\zeta\omega_n 2\gamma\omega_c + \omega_n^2 + \omega_c^2)s^3 \\ &+ (2\zeta\omega_n\omega_c^2 + 2\gamma\omega_c\omega_n^2 - \sigma^2\Gamma_2 + k_t\sigma^2)s^2 \\ &+ (\omega_n^2\omega_c^2 - \sigma^2\Gamma_1 + k_t\sigma^2 2\gamma\omega_c)s + k_t\sigma^2\omega_c^2 \end{aligned} \tag{6}$$

$M_{den}(s)$ can be expressed as:

$$M_{den}(s) = s^5 + K_4 s^4 + K_3 s^3 + K_2 s^2 + K_1 s + K_0 \tag{7}$$

where:

$$\begin{aligned} K_4 =& 2\zeta\omega_n + 2\gamma\omega_c \\ K_3 =& 2\zeta\omega_n 2\gamma\omega_c + \omega_n^2 + \omega_c^2 \\ K_2 =& 2\zeta\omega_n\omega_c^2 + 2\gamma\omega_c\omega_n^2 - \sigma^2\Gamma_2 + k_t\sigma^2 \\ K_1 =& \omega_n^2\omega_c^2 - \sigma^2\Gamma_1 + k_t\sigma^2 2\gamma\omega_c \\ K_0 =& k_t\sigma^2\omega_c^2 \end{aligned} \tag{8}$$

It can be seen that the coefficients of the characteristic polynomial (7) determine the location of the closed-loop poles of the system. The five poles of the closed loop can be therefore placed arbitrarily by choosing the values of the five coefficients K_i.

Then, the parameters of the controllers $C_{damp}(s)$ and $C_{track}(s)$ can be solved recursively from (8) leading to the following expressions:

$$\begin{aligned} 2\gamma\omega_c =& K_4 - 2\zeta\omega_n \\ \omega_c^2 =& K_3 - \omega_n^2 - 2\zeta\omega_n 2\gamma\omega_c \\ k_t =& K_0/(\sigma^2\omega_c^2) \\ \Gamma_2 =& -(K_2 - 2\zeta\omega_n\omega_c^2 - 2\gamma\omega_c\omega_n^2 - k_t\sigma^2)/\sigma^2 \\ \Gamma_1 =& -(K_1 - \omega_c^2\omega_n^2 - 2\gamma\omega_c k_t\sigma^2)/\sigma^2 \end{aligned} \tag{9}$$

In this article the poles of the closed loop system are placed by following the design criteria of [19], where the desired closed-loop performance is defined by a flat band response at low frequencies which rolls off above the resonance frequency. This design criteria is met when the poles of the closed-loop system lie along a circle of radius ω_n and are spaced at equal angular distances as in the low pass Butterworth filter (which is often referred to as a "maximally flat magnitude" filter).

4. Modified PVPF control scheme with delay compensation

In the previous section the equations for designing the traditional PVPF control scheme were presented. It can be seen that these formulas are based on a simplified model of the nanopositioner where the delay is not considered. However, as stated in subsection 2.2, the experimental system has a significant delay. The theoretical model of the platform, therefore, has to be modified in order to include the effects of the delay leading to the following expression:

$$G(s) = \frac{e^{-\tau s}\sigma^2}{s^2 + 2\zeta\omega_n s + \omega_n^2} \tag{10}$$

where τ is the value of the time delay introduced in the system.

When (10) is considered, the equation of the closed-loop transfer function has the following expression: $M'(s) = M'_{num}(s)/M'_{den}(s)$, where:

$$\begin{aligned} M'_{num}(s) =& e^{-\tau s}(s^2 k_t + 2sk_t\omega_c\gamma + k_t\omega_c^2)\sigma^2 \\ M'_{den}(s) =& s^5 + (2\zeta\omega_n + 2\gamma\omega_c)s^4 \\ &+ (2\zeta\omega_n 2\gamma\omega_c + \omega_n^2 + \omega_c^2)s^3 \\ &+ (2\zeta\omega_n\omega_c^2 + 2\gamma\omega_c\omega_n^2 + e^{-\tau s}\sigma^2(k_t - \Gamma_2))s^2 \\ &+ (\omega_n^2\omega_c^2 + (k_t\sigma^2 2\gamma\omega_c - \sigma^2\Gamma_1)e^{-\tau s})s \\ &+ k_t\sigma^2\omega_c^2 e^{-\tau s} \end{aligned} \tag{11}$$

As (11) shows, the effect of the delay is the addition of an infinite number of poles in the closed-loop transfer function, and a change in the location of the five closed-loop poles placed by using the equations

of the traditional PVPF control scheme. Moreover, as the delay is increased, the pair of complex poles closest to the imaginary axis are displaced towards the right half plane, reducing the overall stability of the closed-loop system. Note that since the delay introduced in the system is related to the sampling rate, an upper bound on the maximum admissible delay can be translated to a lower bound for the admissible sampling rate.

It is important to note that, besides the reduction of the stability, the introduction of a delay displaces the location of the five designed poles from the circle with radius ω_n, which means that the design criteria for the PVPF cannot be achieved (flat band response at low frequencies which rolls off above the resonant frequency).

Since the design criteria for the PVPF cannot be achieved for systems with delay, and the stability of the controlled system is also conditioned by the delay, the development of new control design methods to overcome these problems is of utmost interest.

If the relationship (9) is substituted in (11), after some rearrangements the characteristic polynomial of the closed-loop transfer function becomes:

$$\begin{aligned} M'_{den}(s) =& s^5 + s^4K_4 + s^3K_3 \\ &+ s^2[(\omega_n^2(1-4\zeta^2)K_4 + 2\omega_n\zeta K_3 \\ &+ \omega_n^3(8\zeta^3 - 4\zeta)) + e^{-\tau s}(\omega_n^2(4\zeta^2-1)K_4 \\ &- 2\omega_n\zeta K_3 + K_2 + \omega_n^3(4\zeta - 8\zeta^3))] \\ &+ s[(-2\omega_n^3\zeta K_4 + \omega_n^2 K_3 + \omega_n^4(4\zeta^2-1)) \\ &+ e^{-\tau s}(2\omega_n^3\zeta K_4 - \omega_n^2 K_3 + K_1 + \omega_n^4(1-4\zeta^2))] \\ &+ K_0 e^{-\tau s} \end{aligned} \tag{12}$$

Note that the controller coefficients do not appear explicitly in (12). This expression only depends on the plant parameters and the constants $K_i, 0 \leq i \leq 4$. Controller coefficients are embedded in these constants according to (8). The design procedure implies two sequential steps: 1) determining constants K_i that place the closed-loop poles in the desired locations and 2) obtaining controller coefficients from the K_i's by using the inverse relations (9).

For desired closed-loop poles given by $p_i, 1 \leq i \leq 5$, then conditions $M'_{den}(p_i) = 0, 1 \leq i \leq 5$ have to be verified. This can be expressed in a compact matricial form as:

$$A \cdot K = B \tag{13}$$

where $K = (K_0 K_1 K_2 K_3 K_4)^T$, and matrices $B \in \Re^{5x1}$ and $A \in \Re^{5x5}$ only depend on the plant parameters and the desired closed-loop poles, being

$$\begin{aligned} b_i =& -p_i^5 + p_i^2 4\omega_n^3\zeta(e^{-\tau p_i} - 1)(2\zeta^2 - 1) \\ &+ p_i\omega_n^4(e^{-\tau p_i} - 1)(4\zeta^2 - 1) \end{aligned} \tag{14}$$

and

$$\begin{aligned} a_{i,1} =& e^{-\tau p_i} \\ a_{i,2} =& p_i e^{-\tau p_i} \\ a_{i,3} =& p_i^2 e^{-\tau p_i} \\ a_{i,4} =& p_i^3 - 2(e^{-\tau p_i} - 1)\omega_n\zeta p_i^2 - (e^{-\tau p_i} - 1)\omega_n^2 p_i \\ a_{i,5} =& p_i^4 + \omega_n^2(e^{-\tau p_i} - 1)(4\zeta^2 - 1)p_i^2 + 2\omega_n^3\zeta(e^{-\tau p_i} - 1)p_i \end{aligned} \tag{15}$$

where $1 \leq i \leq 5$.

The linear equation (13) can be easily solved by inverting matrix A, which would be full rank if it were verified that $p_i \neq p_j$ for $i \neq j$. Once constants K_i have been obtained, the coefficients of controllers $C_{damp}(s)$ and $C_{track}(s)$ are obtained from (9).

Note that by following this procedure the exact location of five closed loop poles can be defined. However, the transcendentality of the delay brings infinitely many characteristic roots in the closed-loop transfer function. To complete the design procedure it is therefore necessary to determine whether the designed five closed-loop poles are dominant over the infinite remaining poles introduced by the delay, i.e. if the five designed poles are closer to the imaginary axis than the remaining infinite poles of the system. This issue will be studied in Section 7.

5. Experimental setup and system identification

In this section, the hardware utilised to carry out all of the experiments is described. The section also provides details of the system identification procedure.

5.1. Experimental setup

Figure 2 shows the experimental setup used in this work. It consists of a two-axis piezoelectric-stack actuated serial-kinematic nanopositioner designed at the EasyLab, University of Nevada, Reno, USA. It has an input range of ± 100 V resulting in a displacement range of ± 20 μm. Two low-noise, linear voltage amplifiers (PDL200) from Piezodrive, each with an output range of 0 V - 200 V, a variable bias capability of 0 V - 200 V and a fixed voltage gain of 20 are used to supply voltage inputs to the piezoelectric-stack actuators. The displacement is measured by a Microsense 4810 capacitive displacement sensor and a 2805 measurement probe with a measurement range

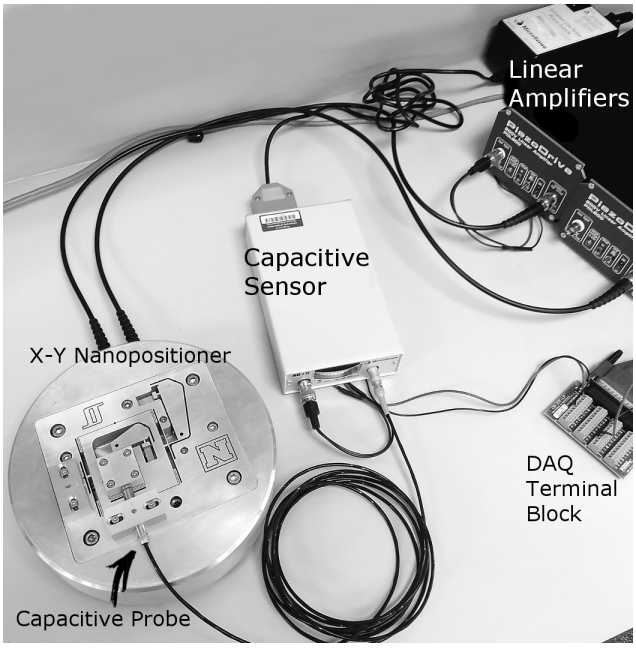

Figure 2. A two-axis serial kinematic nanopositioner, designed at the EasyLab, University of Nevada, Reno, driven by two PiezoDrive 200V Linear amplifiers, with position measured by a Microsense 4810 capacitive sensor

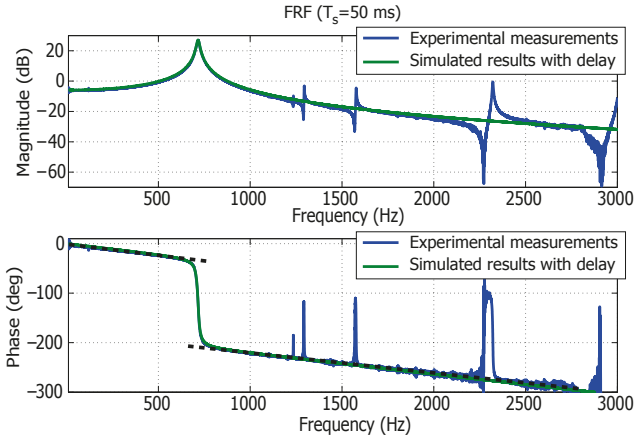

Figure 3. FRF of the experimental platform and the second-order model (including time delay), measured from the input to output displacements

of ± 50 μm for a corresponding voltage output of ± 10 V. A PCI-6621 data acquisition card from National Instruments installed on a PC running the Real-Time Module from LabVIEW is used to interface between the experimental platform and the control design. The PC utilised is an OPTIPLEX 780 with an Intel(R) Core(TM)2 Duo Processor running at 3.167 GHz and equipped with 2GB of DDR3 RAM memory. The whole system is able to achieve deterministic sampling times as low as 30 microseconds.

The PCI-6621 data acquisition card has a maximum sampling rate of 250 kS/s, this is the maximum speed of both the A/D and the D/A converter. The time for a conversion at this rate is 4 μs. Taking into account the additional 10 μs padding added in each A/D and D/A conversions (according to the technical details of the data acquisition drivers of National Instruments (NI-DAQmx)), a single channel of data acquisition will require at least a 14 μs period. Since each cycle is composed of an analog acquisition and an analog generation, the sum of both conversions add up to a total latency of 28 μs per cycle. This latency determines a lower bound on the cycle time achievable by the experimental system of 28 μs (in the experimental setup the lowest cycle time achievable was 30 μs).

The cross-coupling between the two axes was measured leading to a result close to -40 dB. Such a small value justifies the assumption made in Section 2 of considering the effects of cross-coupling negligible in the analysis. The $x-$axis of the platform is used to conduct the experiments presented in this work. However, the $y-$axis was set to 0 V as input to mimic a realistic platform operation.

5.2. Identification of the experimental platform

In this section, the experimental procedure to characterise the dynamics of the nanopositioner and the hardware utilised are presented.

To identify the linear model of the plant, small signal frequency response functions (FRFs) were utilised. The FRFs are determined by applying a sinusoidal chirp signal (from 10 to 5000 Hz) with an amplitude of 0.2 V as input to the voltage amplifier of the $x-$axis and measuring the output signal in the same axis. Subsequently, the FRFs are computed by taking the Fourier transform of the recorded data. It should be noted that, using small amplitudes, the nonlinear effects of the PEAs such as hysteresis can be considered negligible. It should be noted also that, since the capacitive sensor measures relative displacements from a zero point, before each experiment a new zero point is measured in order to avoid any offset in the measurements. In Figure 3 the magnitude and phase responses of the FRF of G(s) are plotted for a sampling time of 50 μs.

The chosen frequency range captures the first four resonance modes of the platform (which supports the theoretical model (2)) and shows the effect of the delay of the system. The presence of a delay can be observed in the phase response of Figure 3, where the phase plot shows a linear behaviour at low and high frequencies (the two dotted lines in Figure 3). This result suggests that the transfer function of the system corresponds to that shown in (10). Note that although four resonance modes have been identified in the measured FRF, only

the first mode is considered in the design of the PVPF control scheme, as the first mode is dominant.

The procedure utilised to obtain the transfer function of the system consists of two steps: first the dominant resonance mode of the transfer function of the system was obtained by using the subspace based modelling technique described in [28], and then the delay was adjusted by minimizing the root mean square error of the phase response.

In order to identify the dependence of the delay on the sampling time, several FRF were obtained for different sampling times, ranging from 30 to 100 μs in increments of 10 μs, and from 100 to 200 μs in increments of 20 μs. The 13 measurements were utilised to identify the following model of the system:

$$G(s) = \frac{1.024 \cdot 10^7 e^{-\tau s}}{s^2 + 99s + 2.025 \cdot 10^7} \tag{16}$$

where the value of τ is determined by the following equation:

$$\tau = \frac{1}{2} T_s + 90 \cdot 10^{-6} \tag{17}$$

where T_s is the sampling time. Both the sampling time T_s and the delay τ are expressed in seconds.

It can be seen that the resonance frequency of the plant is 716.2 Hz, and that there is a linear relationship between the sampling period and the delay introduced in the system. The delay of the system is due to two different phenomena: on the one hand there is a fixed delay of 90 μs determined by the latency of the system (30 μs) and the mechanical design of the nanopositioner (60 μs). On the other hand, there is a delay proportional to half the sampling time as predicted theoretically in [22, 23]. The effects of the different delays associated with each sampling rate are shown in Figure 4, where it can be seen that the slope of the phase response of the system is steeper as the sampling period increases. These figures also show that the identified model accurately fits the experimental results.

6. Experimental results

In this section, the experimental results obtained applying the traditional and the modified PVPF control scheme are presented. It is shown that, with the modified PVPF control scheme, the maximum delay admissible in the plant before encountering instability is greater than that observed using the traditional PVPF design, which allows the utilisation of slower sampling rates and cheaper equipment without a meaningful loss of performance.

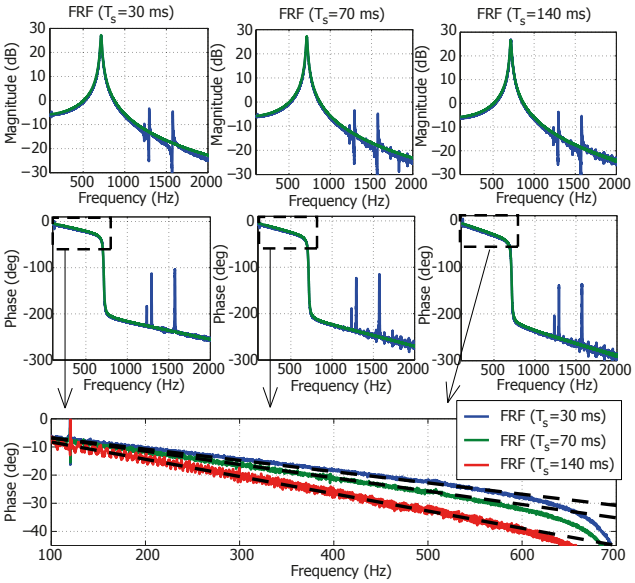

Figure 4. Magnitude and phase response of the nanopositioning platform measured from input to output displacement for different sampling rates. Plots in blue are experimental results and plots in green are simulated results including time delay

6.1. Experimental results with the traditional PVPF control scheme

Neglecting the delay present in the nanopositioning system can lead to performance degradation and stability issues in closed-loop operation. In this article, the PVPF controller is utilised to illustrate these issues. Using the method described in Section 3 and [19] to derive the controller parameters, the resulting PVPF and tracking controllers are given by:

$$C_{damp}(s) = \frac{-15040s + 68110000}{s^2 + 14460s + 84350000} \tag{18}$$

$$C_{track}(s) = \frac{2136}{s} \tag{19}$$

However, when the designed controller is applied to the experimental platform, the results obtained are very different from the design criteria and from those produced by simulation of the ideal case, i.e. without delay in the plant. Figure 5 shows the magnitude response of the simulated closed-loop system (without delay), and the experimentally measured magnitude response for different sampling times (note that each sampling time has a different associated delay determined by (17)). It can be seen that the experimental results are not consistent with those achieved by simulation (without delay). Consequently, the design criteria is not met.

It is observed that the experimental response does not achieve a flat band response, and that the 3 dB bandwidth of the system is significantly lower than that

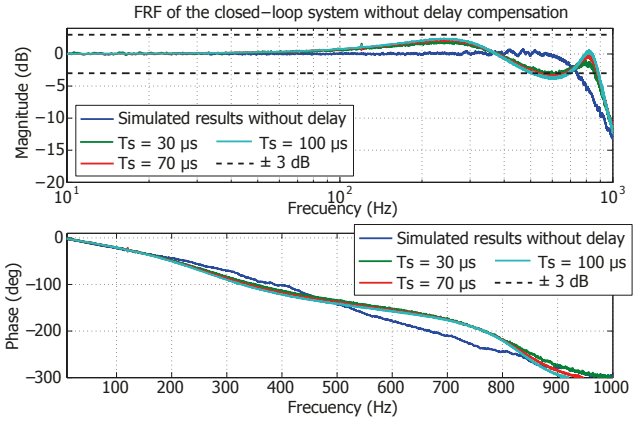

Figure 5. Frequency response of the experimental system without delay compensation and simulated results for the ideal case (without delay)

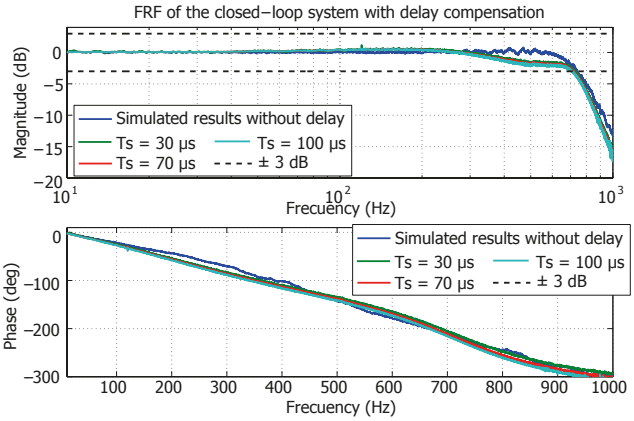

Figure 6. Frequency response of the experimental system with delay compensation and simulated results for the ideal case (without delay)

achieved in simulation. Note that the experimentally measured bandwidth varies with sampling time, e.g. 538.9 Hz (30 μs), 526.6 Hz (70 μs), 503.4 Hz (100 μs). It can be seen that even in the most favorable case (with a sampling time of 30 μs) the bandwidth is very far from the resonance frequency. It can also be seen that, as the sampling time is increased, and consequently the delay associated with it, the performance of the system deteriorates. The presence of the delay displaces the five designed poles from their original locations. Since these poles no longer lie in the Butterworth pattern, the maximally flat magnitude response cannot be achieved.

6.2. Experimental results with the modified PVPF control scheme

In this section, the effect of the delay is considered in the design of the control scheme by using the modified PVPF proposed in this article.

Figure 6 shows the experimentally measured magnitude response of the closed-loop system for various sampling times and the simulated magnitude response for the ideal case (without delay). The modified PVPF control scheme is redesigned for each specific sampling time, to reduce the effects of the associated delay.

It can be seen that the experimental results more closely match the desired flat band response than is the case when the delay is not considered. It is also observed that the 3 dB bandwidth of the closed loop system is significantly higher than that achieved using traditional PVPF, e.g. 711.3 Hz (30 μs), 707.2 Hz (70 μs), 707.2 Hz (100 μs), (this can be seen graphically by comparing Figure 5 and Figure 6). Note that as the sampling time is increased the deterioration in the performance of the controller is lower than with the traditional PVPF.

7. Analysis of the results

The modified PVPF scheme achieves better performance than the traditional PVPF when applied to systems with time delay. Additionally, the modified PVPF can be applied to a wider range of systems with different delays associated, and presents improved robustness to uncertainties in the delay of the system. In this section, the identified model of the experimental platform is utilised to illustrate, with numerical values, the advantages of the modified PVPF over the traditional PVPF.

In order to deal with the issue of having an infinite number of poles introduced by the delay (and in order to simplify the analyses performed in this section), it is desirable to represent an equivalent low degree rational transfer function that approximates the behaviour of the delay of the system. The typical method to approximate the effect of the delay is the Padé approximation [29]. The Padé approximation technique has some useful features such as the computational simplicity and the fitting of time-moments. The poles introduced by Padé approximation in the closed-loop transfer function can be utilised therefore to check if the designed five closed-loop poles are dominant over the poles introduced by the delay.

A second order Padé approximation of the delay is utilised in this work to compute the placement of the poles of the closed-loop system, and to ensure the designed poles of the controller are dominant. The Padé approximation is defined as [30]:

For $n > 1$, the $[n, n]$ Padé approximant is given by:

$$e^{-\tau s} = \frac{p(-s)}{p(s)} \tag{20}$$

where

$$p(s) = \sum_{k=0}^{n} \binom{n}{k} \frac{(2n-k)!}{(2n)!} s^k. \tag{21}$$

When the second order Padé approximation is utilised to substitute the exponential terms in the transfer function of the closed-loop system, the resulting characteristic equation consists of seven poles (five poles are determined by the parameters of the controller utilised and new two poles introduced by the second order Padé approximation are determined by the delay of the system).

7.1. Range of application of the proposed method

As stated in section 4, the last stage in the design of the modified PVPF control scheme is to ensure the five designed poles (which lie along a circle of radius ω_n, as consequence of the design procedure) are dominant over the poles introduced by the delay. In this paper, the five designed poles are considered dominant if their proximity to the imaginary axis is greater than that of the poles introduced by delay.

Since the delay introduces an infinite number of closed-loop poles, the second order Padé approximation is utilised in order to compute only a finite number of roots of the closed-loop system. It is assumed that any meaningful pole introduced by the delay would be situated further from the imaginary axis than those introduced by the Padé approximation. Assuming this hypothesis, the dominance of the five designed poles only needs to be checked over a finite number of poles (only two in our case).

The position of the closed-loop poles of the whole system is shown in Figure 7, for increasing delay in the range $\tau = [0, 600]$ μs. It can be seen that the five designed poles always lie in the same position (since a new controller has been computed for each value of the delay). However, the remaining two poles introduced by the Padé approximation are displaced, moving towards the imaginary axis as the delay is increased. This result suggests an upper limit on the maximum permissable delay, in this case $\tau = 351$ μs. Any value of delay greater than $\tau = 351$ μs places the poles introduced by the Padé approximation closer to the imaginary axis than some of the designed poles.

It was verified through simulation that the effect of the poles introduced by the delay is non-negligible in systems where the delay exceeds the maximum range of application ($\tau = 351$ μs). This determines that the maximally flat magnitude response cannot be achieved with the proposed method when the delay is greater than $\tau = 351$ μs.

It is important to note that, from a practical point of view, the lower bound on the range of stability is not meaningful since these limits depend on the nominal

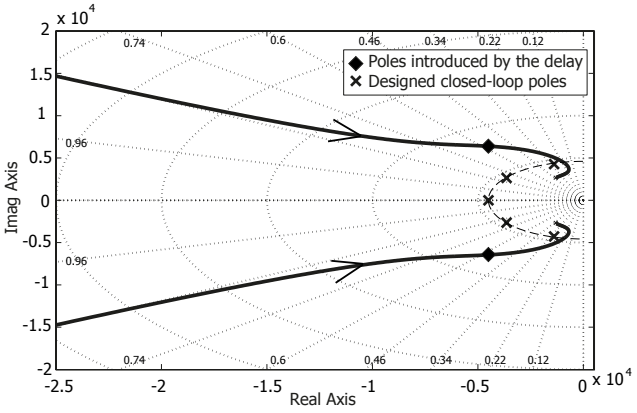

Figure 7. Evolution of the closed-loop poles of the experimental platform for delay in the range [0,600] μs. The position of the poles for a delay of 351 μs is indicated with crosses and diamonds.

time delay used in the controller design. For example, for a nominal time delay of $\tau = 254$ μs, this range of stability becomes $\tau = [0, 613]$ μs.

It was experimentally confirmed that the slowest admissible sampling frequency, in order to control the system, is determined by 10 times the resonant frequency. Therefore, the maximum sampling time T_s^{max} is determined by the following expression:

$$T_s^{max} = \frac{1}{716.2 \cdot 10} \simeq 140 \ \mu s \tag{22}$$

Since sampling times greater than $T_s = 140$ μs cause the system to become unstable, only values of delay as high as $\tau = 160$ μs can be achieved (see (17)). In this case, the instability of the closed-loop experimental platform is caused by the fact that the sampling rate is not fast enough to capture the first resonant mode, not because of the problem studied here, relating to the delay. This prevents the theoretical ranges of admissible delay computed in this section from being experimentally validated.

7.2. Stability robustness

In this subsection, the maximum admissible difference between the nominal delay (the value used in the controller design) and the actual delay of the system, in both the traditional and modified PVPF control schemes, is analysed. Unlike in the previous subsection, in which a new controller was designed for each value of delay, the control scheme is designed, as in Sections 3 and 4, and the delay increased until the system becomes unstable.

In order to analyse the traditional PVPF controller, the controller designed in (18) and (19) is utilised. Applying this controller to the simulated model of the plant, the delay is varied in the range

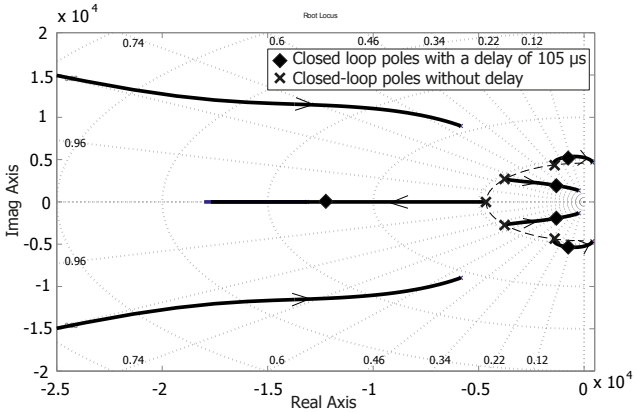

Figure 8. Root contours of the closed-loop system controlled with the traditional PVPF when the changing parameter is the delay of the system (Circle of radius ω_n indicated in dashed line)

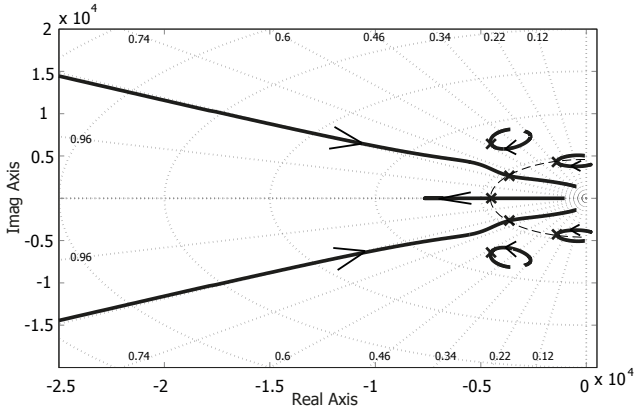

Figure 9. Root contours of the closed-loop system controlled with the modified PVPF scheme scheme designed considering a nominal value of delay $\tau = 351$ μs (indicated with crosses). The arrows in the figure indicate the moving direction of the poles when the actual delay of the plant is increased

$\tau = [0, 600]$ μs and the root contours of the closed loop system are plotted in Figure 8.

It can be seen that, as the delay is increased, the five designed poles are displaced from their initial location in the circle of radius ω_n (indicated by the dashed line). It is important to note that even for small values of delay such as 105 μs (which is associated with the highest experimentally achievable sampling frequency) the position of the poles is highly distorted. For delay greater than $\tau = 250$ μs a pair of complex poles are displaced to the right half-plane, leading to an unstable system. Therefore, the traditional PVPF can guarantee the stability of the system only for values of delay $\tau \leq 250$ μs.

The modified PVPF can produce different controllers depending on the value of the nominal delay considered in the design stage. In order to reproduce the worst-case scenario as in the analysis of the traditional PVPF, the controller is designed taking the upper limit of the range of application as nominal value of delay.

Figure 9 depicts the evolution of the poles of the closed-loop system with the modified PVPF control scheme designed considering a nominal delay of $\tau = 351$ μs. In order to compute the evolution of the closed-loop poles, the actual delay of the plant is varied in the range $\tau = [0, 800]$ μs.

It can be seen that as the difference between the actual value of the delay and the nominal value is increased, the distance of the closed-loop poles from the circle of radius ω_n is also increased. Whether the delay is too small or too large, the system can become unstable. It is found that the system is stable for delay in the range $\tau = [107, 755]$ μs.

It is important to note that, from a practical point of view, the lower bound of the range of stability is not meaningful, since if the delay is lower than $\tau = 351$ μs a different controller can be designed which guarantees a maximally flat magnitude response.

From these results it can be seen that the maximum admissible value of delay for each controller in the worst-case scenario (and without taking into account the sampling constraint (22) imposed by the first natural frequency of the nanopositioner) are: $\tau = 250$ μs for the traditional PVPF, and $\tau = 755$ μs for the modified PVPF. This means that the proposed methodology can increase, by 3 times, the maximum delay admissible which ensures system stability, with respect to the value given by the traditional PVPF.

8. Conclusions

This paper has proposed a new methodology to tune the parameters of the well-known PVPF control scheme, which allows to place arbitrarily the dominant closed-loop poles of the system, even in the presence of a time delay in the nanopositioning system. It has been experimentally and theoretically shown that the delay introduced in the nanopositioner is determined by the sampling rate utilised and its effects cannot be neglected. It has also been demonstrated that the performance of the traditional PVPF is greatly affected by the time delay introduced by the controller, i.e. the system performance deteriorates as the sampling time is increased.

The experimental results and the analysis of Section 7 show that the modified PVPF achieves better performance in the presence of a time delay and, higher stability robustness that the traditional PVPF. It has also been demonstrated that, unlike the traditional PVPF (in which the response is deteriorated by any delay), the proposed controller can produce an ideal response under a wide range of admissible values of delay, and sampling times. These results determine the

potential utilisation of the modified PVPF with slower sampling rates, which would allow the utilisation of cheaper equipment for the electronic control circuitry, and would reduce the overall cost of the system.

Furthermore, the proposed methodology and the proposed theoretical model of the nanopositioner which includes the effects of the delay could be utilised in future works to extend other widely utilised control schemes such as PPF, and IRC controllers.

Acknowledgments

This paper was sponsored by the Spanish FPU12/00984 Program (Ministerio de Educacion, Cultura y Deporte). It was also sponsored by the Spanish Government Research Program with the Project DPI2012-37062-CO2-01 (Ministerio de Economia y Competitividad) and by the European Social Fund.

References

[1] Andrew J. Fleming and Kam K. Leang. *Design, Modeling and Control of Nanopositioning Systems*. Advances in Industrial Control. Springer International Publishing, 2014.

[2] Santosh Devasia, E. Eleftheriou, and S. O R Moheimani. A survey of control issues in nanopositioning. *Control Systems Technology, IEEE Transactions on*, 15(5):802–823, Sept 2007.

[3] U-Xuan Tan, Win Tun Latt, Cheng Yap Shee, and Wei Tech Ang. A low-cost flexure-based handheld mechanism for micromanipulation. *IEEE/ASME Transactions on Mechatronics*, 16(4):773–778, Aug. 2011.

[4] Zhenhua Wang, Liguo Chen, and Lining Sun. An integrated parallel micromanipulator with flexure hinges for optical fiber alignment. In *Mechatronics and Automation, 2007. ICMA 2007. International Conference on*, pages 2530–2534. IEEE, Aug. 2007.

[5] Rachel A. Oliver. Advances in afm for the electrical characterization of semiconductors. *Reports on Progress in Physics*, 71(7):076501, Jul. 2008.

[6] Noriyuki Kodera, Hayato Yamashita, and Toshio Ando. Active damping of the scanner for high-speed atomic force microscopy. *Review of Scientific Instruments*, 76(5):–, 2005.

[7] Toshio Ando, Takayuki Uchihashi, Noriyuki Kodera, Daisuke Yamamoto, Atsushi Miyagi, Masaaki Taniguchi, and Hayato Yamashita. High-speed afm and nano-visualization of biomolecular processes. *Pflgers Archiv - European Journal of Physiology*, 456(1):211–225, Apr. 2008.

[8] M. J. Rost, G. J. C. van Baarle, A. J. Katan, W. M. van Spengen, P. Schakel, W. A. van Loo, T. H. Oosterkamp, and J. W. M. Frenken. Video-rate scanning probe control challenges: setting the stage for a microscopy revolution. *Asian Journal of Control*, 11(2):110–129, Mar. 2009.

[9] Kam K. Leang and Andrew J. Fleming. High-speed serial-kinematic afm scanner: Design and drive considerations. In *American Control Conference, 2008*, pages 3188–3193. IEEE, Jun. 2008.

[10] J. L. Fanson and T. K. Caughey. Positive position feedback-control for large space structures. *AIAA J.*, Apr. 1990.

[11] B. Bhikkaji, M. Ratnam, and S. O. R. Moheimani. PVPF control of piezoelectric tube scanners. *Sensors Actuators A-Phys.*, 132(2):700–712, Apr. 2007.

[12] H R Pota, S. O. Reza Moheimani, and Matthew Smith. Resonant controllers for smart structures. *Smart Materials and Structures*, 11(1):1–8, Feb. 2002.

[13] S. Salapaka, A. Sebastian, J. P. Cleveland, and M. V. Salapaka. High bandwidth nano-positioner: A robust control approach. *Rev. Scientific Instruments*, 73(9):3232–3241, Sep. 2002.

[14] Sumeet S. Aphale, Andrew J. Fleming, and S. O. Reza Moheimani. Integral resonant control of collocated smart structures. *Smart Materials and Structures*, 16(2):439–446, Apr. 2007.

[15] Sachin P Wadikhaye, Yuen K. Yong, Bharath Bhikkaji, and S. O. Reza Moheimani. Control of a piezoelectrically actuated high-speed serial-kinematic afm nanopositioner. *Smart Materials and Structures*, 23(2):025030, Feb. 2014.

[16] Li Shengquan, Li Juan, Zhang Kezhao, and Mo Yueping. Output prediction based active disturbance rejection control approach and its application in structural vibration. In *Control Conference (CCC), 2014 33rd Chinese*, pages 3614–3619, Jul. 2014.

[17] Andrew J. Fleming. Nanopositioning system with force feedback for high-performance tracking and vibration control. *IEEE/ASME Transactions on Mechatronics*.

[18] Yuen K. Yong, Andrew J. Fleming, and S.O.R. Moheimani. A novel piezoelectric strain sensor for simultaneous damping and tracking control of a high-speed nanopositioner. *IEEE/ASME Transactions on Mechatronics*, 18(3):1113–1121, Jun. 2013.

[19] Douglas Russell, Andrew J. Fleming, and Sumeet S. Aphale. Simultaneous optimization of damping and tracking controller parameters via selective pole placement for enhanced positioning bandwidth of nanopositioners. In *American Control Conference (ACC), 2014*, pages 2184–2189. IEEE, Jun. 2014.

[20] X. B. Chen, Q. S. Zhang, D. Kang, and W. J. Zhang. On the dynamics of piezoactuated positioning systems. *Review of Scientific Instruments*, 79(11):–, 2008.

[21] Andrew J. Fleming. Techniques and considerations for driving piezoelectric actuators at high-speed. In *in Proc. SPIE Smart Materials and Structures*, 2008.

[22] K. Janschek. *Mechatronic Systems Design: Methods, Models, Concepts*. Springer, 2011.

[23] Phillips P.L. and Nagle H.T. *Digital Control System Analysis and Design*. Prentice Hall, 1995.

[24] Arnfinn A. Eielsen, Marialena Vagia, J. Tommy Gravdahl, and Kristin Y. Pettersen. Damping and tracking control schemes for nanopositioning. *IEEE/ASME Transactions on Mechatronics*, 19(2):432–444, Apr. 2014.

[25] Guo-Ying Gu, Li-Min Zhu, Chun-Yi Su, and Han Ding. Motion control of piezoelectric positioning stages: Modeling, controller design, and experimental evaluation. *IEEE/ASME Transactions on Mechatronics*, 18(5):1459–1471, Oct. 2013.

[26] Graham C. Goodwin, S.F. Graebe, and M.E. Salgado. *Control System Design*. Prentice Hall, 2001.

[27] Sumeet S. Aphale, B. Bhikkaji, and S. O R Moheimani. Minimizing scanning errors in piezoelectric stack-actuated nanopositioning platforms. *Nanotechnology, IEEE Transactions on*, 7(1):79–90, Jan. 2008.

[28] T. McKelvey, H. Akcay, and L. Ljung. Subspace-based multivariable system identification from frequency response data. *Automatic Control, IEEE Transactions on*, 41(7):960–979, Jul 1996.

[29] Y. Shamash. *Order reduction of linear systems by Padé approximation methods*. 1973.

[30] Jonathan R. Partington. Some frequency-domain approaches to the model reduction of delay systems. *Annual Reviews in Control*, 28(1):65 – 73, 2004.